TURBULENCE INTENSITY MEASUREMENTS ACROSS A NGV COOLED CASCADE WITH REPRESENTATIVE LEAN BURN COMBUSTOR OUTFLOW

T. Bacci - A. Picchi - T. Lenzi - B. Facchini

DIEF - Department of Industrial Engineering of Florence
University of Florence
50139, via S. Marta 3, Florence, Italy
tommaso.bacci@htc.unifi.it

ABSTRACT

Significant turbulence levels can be achieved at the exit of modern lean-burn aeroengine combustors, due to the limited interaction between swirling mainflow and liner flows. In this study, hot wire anemometry was exploited to assess the turbulence intensity across a film-cooled NGV cascade, installed downstream of a non-reactive lean burn combustor simulator. The interpretation of the turbulence measurements was improved thanks to the average flow field and pressure results, gathered by five hole probe investigation. The results showed that the swirling mainflow was responsible for very high turbulence intensities on the combustor exit plane. Important turbulence intensities were also found at the NGV exit, due to the conservation of the residual swirling structure and to its interaction with the endwall flows. The effect of nozzle film-cooling injection was also assessed: a limited effect was found, with film-cooling injection generally leading to slightly reduced turbulence intensities.

KEYWORDS

Turbulence, Hot Wire Anemometry, Five Hole Probe, Lean-Burn Combustors, Aeroengine

NOMENCLATURE

ax, x, y	Spatial coordinates $[m]$	r	Radial coordinate $[m]$
C_{ax}	Axial chord $[m]$	f	frequency $[Hz]$
C_p	Pressure loss coefficient $[-]$	p	Tangential NGV pitch $[^\circ]$
E	Voltage $[V]$	ρ	Density $[kg/m^3]$
η_r	Recovery factor $[-]$	S	NGV pitch at midspan $[mm]$
h	Local annulus height $[m]$	T	Temperature $[K]$
H	Annulus or NGV height $[m]$	t	Tangential coordinate $[^\circ]$
k	Wave number $[m^{-1}]$	Tu	Turbulence intensity $[-]$
MFR	NGV-mainstream mass flow ratio $[\%]$	V	Velocity $[m/s]$

Subscripts	
0	Total
40	Plane 40
41	Plane 41
av	Mass-averaged
eff	Effective
f	Flow
rms	Root-mean-square
w	Sensor wire

Acronyms	
$5HP$	5-hole probe
HWA	Hot Wire Anemometry
NGV	Nozzle Guide Vane
PS	Pressure Side
PVC	Precessing Vortex Core
RQL	Rich-Quench-Lean
SAS	Scale Adaptive Simulation
SS	Suction Side
TKE	mass flux Turbulent Kinetic Energy

INTRODUCTION

Turbulence intensity generated in the combustion chamber significantly influences the turbine aerodynamics and heat transfer. Nasir et al. (2009) showed that the large scale free-stream turbulence promotes a slightly earlier boundary layer transition on the suction surface; an enhancement in heat transfer, on both suction and pressure sides, was found by Radomsky and Thole (1999). Turbulence affects also the nozzle film cooling behaviour (Ekkad and Han (2000)) and the dissipation of the hot streaks coming from the combustor (Jenkins et al. 2004).

In this context, the knowledge of the turbulence intensity and of the unsteady characteristics expected at combustor-turbine interface is crucial to adequate nozzle guide vane design. While, in most of the above mentioned proof of concept studies, turbulence was promoted by the use of grids or air injection, some more representative investigations have been carried out on real combustor hardware operated in isothermal conditions (Fossen and Bunker 2001) or with turbulence generators that resembled combustor liners (Ames 1994, 1997).

Concerning modern aero-engine lean burn combustors, very high degree of swirl are normally expected, due to short axial dimensions of the combustion chamber and limited interaction between main and liner flows. Accurate measurements in reactive environments are made difficult by the harsh conditions, while, for non-reactive test simulators, additional challenges arise due to the complexity of designing a rig with representative swirling flows, without the effect of the combustion process (Hall et al. 2013; Schmid et al. 2014). Moreover, the reliability of conventional measurement techniques for turbulence intensity, like hot wire anemometry (HWA), is significantly challenged by highly three-dimensional flow fields (Kergourlay et al. 2006; Huu and Beguier 1995; Pena and Arts 1994).

For all these reasons, in the open literature few works deal with turbulence measurements across a cascade with representative swirl conditions (Werschnik et al. 2017). The collection of additional experimental data, with a proper benchmarking of the adopted technique, is, therefore, mandatory in order to deepen the knowledge of the behaviour of a realistic turbulence intensity field across NGVs, in the view of supporting an accurate design of the high pressure turbine.

In this work, an experimental campaign on a non-reactive combustor simulator with a film-cooled NGV cascade was carried out. The focus is placed on the evaluation of the turbulence intensity on both the NGV inlet and outlet planes, traversing hot wire anemometry probes. Split-fiber probes were adopted for such a goal. Five hole probe results from the work of Bacci et al. (2018b) will be also reported, in order to both provide information regarding the overall flow field at NGV inlet/exit and to assess the capability of the adopted HWA technique to deal with a highly 3D flow field.

TEST RIG

The test campaign was carried out on a non-reactive test rig composed by a three-sector combustor simulator equipped with a high-pressure NGV cascade as shown in Fig. 1a. The simulator was designed to capture all physical scales at the combustor-turbine interface, with the goal of replicating a modern

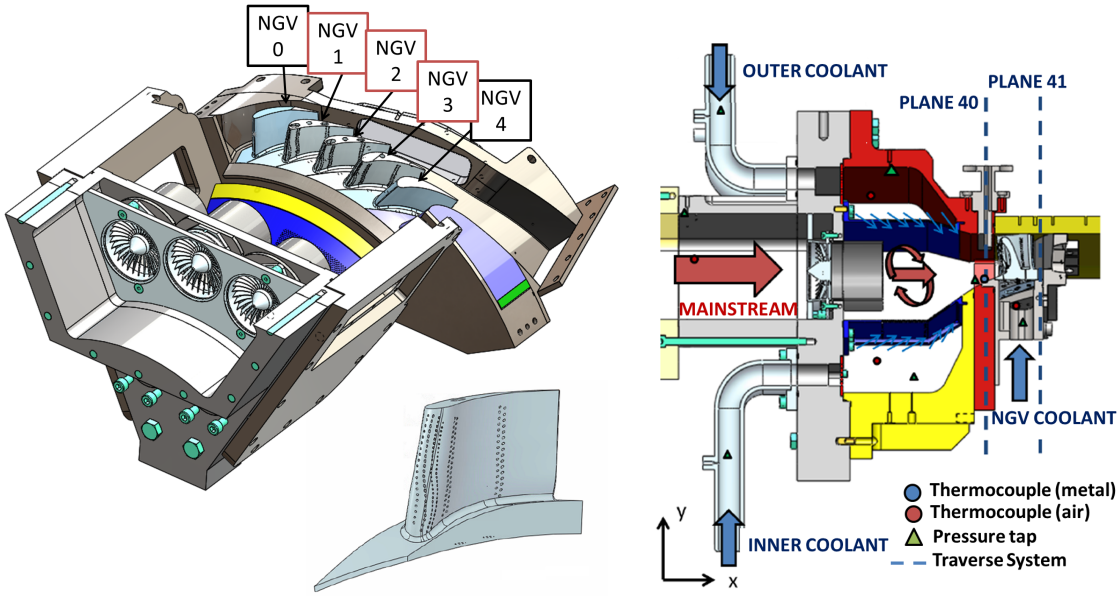

(a) (b)

Figure 1: Trisector rig layout: 3D CAD model (a) and sectional view (b)

lean burn combustor configuration. The three sector configuration was adopted to make the central sector flow field less sensitive to the presence of the lateral walls. Details of the CFD-aided design process and of its experimental verification can be found in the works of Bacci et al. (2018b) and Koupper et al. (2014).

In the test rig sectional view (Fig. 1b), red and blue arrows represent main and coolant flows respectively. The mainflow can be heated up to about 260 °C and then reaches the combustor simulator through three axial swirlers, while two separate cooling flows feed the liners effusion systems; no dilution holes are present. The swirlers design was aimed at creating a representative flow field even without the effect of the combustion process. Ducts of 55mm length ($\approx 35\%$ of the total chamber length) were installed on the swirlers, to preserve the swirling mainflow from the interaction with the cooling flows (Bacci et al. 2015; Andreini et al. 2016). The chamber is characterized by a short distance between the inlet plane and the NGV position ($\approx$ 2.5 times the swirlers diameters) and the inner liner is strongly convergent towards the final part of the chamber with respect to the horizontal axis (Fig. 1b). The test rig has a NGV module made by six high pressure vane passages, to achieve a vortex-to-vane count ratio of 1:2; the central airfoil is aligned with the central swirler, while the adjacent ones are positioned halfway between two swirlers. The three central NGV airfoils (NGV_{1-3}) are film-cooled, according to Fig. 1a, since only the rig central sector, corresponding to two vane pitches, is the measurements domain. A CAD model of the NGV airfoil is shown in Fig. 1a: the tip is at a 280mm radius, while the first part of the inner endwall has a convergent shape. Referring to the constant-height part of the NGVs, they are characterized by an aspect ratio (H/C_{ax}) of 1.04 and a midspan pitch-chord ratio (S/C_{ax}) of 1.06. the NGV exit flow angle is about 74°, even if it is not completely constant through the airfoil height. The film cooling scheme is made by 8 rows of cylindrical film cooling holes, with four shower head and four pressure side rows. More details on the combustor simulator rig and on NGVs film cooling system can be found in Bacci et al. (2018) and Bacci et al. (2018b).

To carry out the targeted measurement campaign, the test rig is provided with two accesses for probe traversing, depicted in Fig. 1b. The first one allows the investigation of the combustor simulator exit plane, called *Plane 40*, 0.5 axial chords upstream the NGV leading edges, while the second, called *Plane 41*, is located 0.25 axial chords downstream the trailing edge and corresponds to the nominal NGV exit

Flow split: swirlers-liners	65%-35%
MFR (film cooling mass flow / mainstream mass flow)	7.5%-3.5%-0%
Chamber pressure	127 kPa
Flow temperatures: Swirler - Liner coolant - NGV coolant	300 - 300 - 300 K
Swirler Reynolds number	168500
Swirler Mach number	0.098
Plane 40 Mach number	0.0997
Plane 41 Mach numbers at MFR=7.5% (0%)	0.7 (0.68)

Table 1: Isothermal operating points conditions

plane.

Operating conditions

In order to perform hot wire anemometry measurements, an isothermal room-temperature operating point had to be adopted (mainflow heater switched off). The operating conditions were set with the goal to match the main non dimensional parameters affecting mainstream, cooling flows and their mutual interactions. In particular the swirler mass flow and combustor chamber pressure were set to have representative Reynolds and Mach number, while the effusion flow trough the liners and the NGVs cooling flow were regulated imposing nominal mass flow splits. At nominal condition, the NGVs cavities were fed with a cooling flow equal to 7.5% of the total main mass flow approaching each cooled passage. The resulting blowing ratio, excluding the shower head, is between 0.9 and 2 for the different cooling rows. In addition, a condition without coolant and an in-between condition ($MFR = 3.75\%$) were explored to evaluate the effect of the NGV coolant mass flow rate on the results. A summary of the operating conditions is shown in Table 1, while the row-by-row BR calculation at nominal condition is reported in Bacci et al. (2018). It is worth to underline that the exit Mach number of the cascade is relative lower respect to actual engine conditions: even if for instance local sonic conditions could have an impact on the final results, the general conclusions of the paper can be considered valuable to better understand the Tu behaviour across cooled NGVs and the impact of cooling flows.

EXPERIMENTAL TECHNIQUE AND DATA REDUCTION

As stated in the introduction, the results reported in this treatment have been collected by means of five hole probe and hot wire probes traversing on the NGV inlet/outlet planes. Since a thorough characterization of the five hole probe setup can be found in the work of Bacci et al. (2018), very little space will be left to its description in this treatment. On the other hand, the setup of HWA measurements, that are the actual goal of this paper, will be deeply detailed in the following. Both kinds of probes have been traversed using an automatic traverse system. The investigated plane at NGV inlet is slightly different from HWA to 5HP; while for the first one it corresponds to the nominal Plane 40, the measurement position of the latter had to be slightly moved upstream (≈5.8mm, 14.5% of the NGV axial chord), due to the cobra shape of the probe. On the other hand, at the exit plane the positions are exactly the same (i.e. Plane 41), since it was possible to insert the pneumatic probe slightly downstream of the hot wire.

Five hole probe technique

A *Vectoflow GmbH* cobra five-hole probe was traversed on the measurement planes, thanks to an automatic, cartesian traverse system. Before the tests, a calibration process was carried out, with a calibration apparatus that allows to explore swirl angles up to $\pm 75^\circ$ and pitch angles up to $+75^\circ/-60^\circ$, while a set of Mach numbers were imposed up to 0.9. The calibration showed that, to achieve reliable results the swirl angle had to be limited within $\pm 30^\circ$; as far as the swirl stays in these limits, the pitch

angle is correctly measured within all the calibrated range. Therefore, Plane 40 measurements were carried out imposing a preswirl of either $+28^\circ$ or -28° to the probe; on Plane 41, a preswirl equal to the average NGV exit angle was chosen. The expected uncertainties are around $\pm 1^\circ$, for flow angles measurements and 2% for pressure.

HWA technique

The HWA measurement technique selected within this application is somehow similar to the one described by Huu and Beguier (1995), who used an X-wire probe with two different orientations, to resolve the three-dimensional flow field. In this work *Dantec Dynamics* split fiber probes were used due to their wider angular acceptance (up to $\pm 90^\circ$ according to the vendor), required for the very high flow angles expected on Plane 40. Other HWA techniques generally adopted for highly 3D flow fields, like the rotating slanted single wire, could not be adopted because the expected turbulence intensities were too high to allow higher order terms to be neglected.

Dual sensor split fibers are made by a 3mm long quartz cylinder with a 200 μm diameter, where two identical nickel film sensors, with a 1.25 mm active length, are deposited, as sketched in the top central of Fig. 2. These probes have been developed to investigate 2D flow fields with no velocity components parallel to the quartz cylinder and relevant errors can arise when a third velocity component is added. To overcome this issue and to correctly estimate the three velocity components for each test point, two different probes are used: probe 55R56 was used with the primary goal of evaluating the velocity field on plane y-z (see Fig. 2 for axis notation), while probe 55R57 was employed for plane x-z. The main challenges of the data-reduction procedures were related to the necessity to account for the flow compressibility and for the velocity component that is parallel to each probe wire, especially for Plane 40, where very high flow angles were expected.

Before the tests, a thorough calibration process was performed using a dedicated flow stand that allowed the set the probes orientation by acting on two perpendicular axis and to adjust the flow conditions by regulating the total pressure and temperature of the calibration airflow. Both probes responses were differentiated in "mass-flux" and "angular" response. For the first one, the flow velocity, on the plane normal to the probe wire, was related to the sum of the sensors voltages. A Nu-Re response approach was adopted in order to account for the effects of flow density and temperature. The calibration Reynolds number was calculated starting from the known calibration airflow velocity, pressure and temperature; the sensor wire diameter was used as the characteristic length. The Nusselt number was calculated from the acquired voltages using Eq. 1. The temperature of the sensors working in CTA mode (T_w) were evaluated through the procedure described by Cukurel et al. (2012): runs were repeated varying the calibration airflow temperature; the tested values of temperature and flow velocity were chosen in order to explore all the Reynolds and Mach numbers range expected during the tests. Since the Nu-Re response should be insensitive to the the air and sensor temperatures, T_w was evaluated as the value that made the different calibrations collapse on a unique Nu-Re response. The optimum result was evaluated as the best least square fitting of an exponential Nu-Re curve. In the same way, the choice to consider the temperature of the flow (T_f) as the product of recovery factor (η_r) and the total temperature (T_0), was adopted as it led to the best fitting of the different calibration runs. The same choice was made by Cukurel et al. (2012).

$$Nu = \frac{E_1^2 + E_2^2}{k(T_w - \eta_r T_0)} \tag{1}$$

On the other hand, the "angular response" was characterized by relating the flow angle in the plane orthogonal to the probe wire to Re_i/Re_{eff}. The parameter Re_i was calculated from Nu_i, adopting the same Nu-Re relation developed from the mass flux calibration but using either E_1 or E_2 for the evaluation of Nu_i, through Eq. 1. Since, as expected, both responses suffer from the effect of the velocity component parallel to the cylinder (i.e. the second flow angle) and are strongly modified by it,

several curves have been developed for different "out-of-plane" angles. The calibration was conducted up to swirl angles of $\pm 75°$ and pitch angles up to $-50°/+60°$ with step of $5°$ for each angles, while a set of Mach numbers were imposed up to 0.9, to cover the expected conditions during the tests.

The test execution and data post-processing procedure, summarized in Fig. 2, is based on aligning, point by point, the 55R56 probe with the expected time-average swirl angle (i.e. flow angle on the x-z plane). Thanks to this positioning approach, it was possible to significantly limit the actual flow angles "felt" by the probes and define a data post process based on an iterative procedure, using the calibration curves at swirl = $0°$ for the first iteration step: if the calculated swirl angle at the end of the first step significantly deviated from zero it was possible to go back to the start of the procedure and iterate, selecting a different calibration curve for probe 55R56. The Mach number, for the calculation of the recovery factor through correlations, as well as the swirl angle for the pre-swirl definition, were taken, for each mesh point, from five hole probe results on time averaged basis. The slight difference in the measurement position on Plane 40, between HWA and 5HP, does not result in an actual issue for this

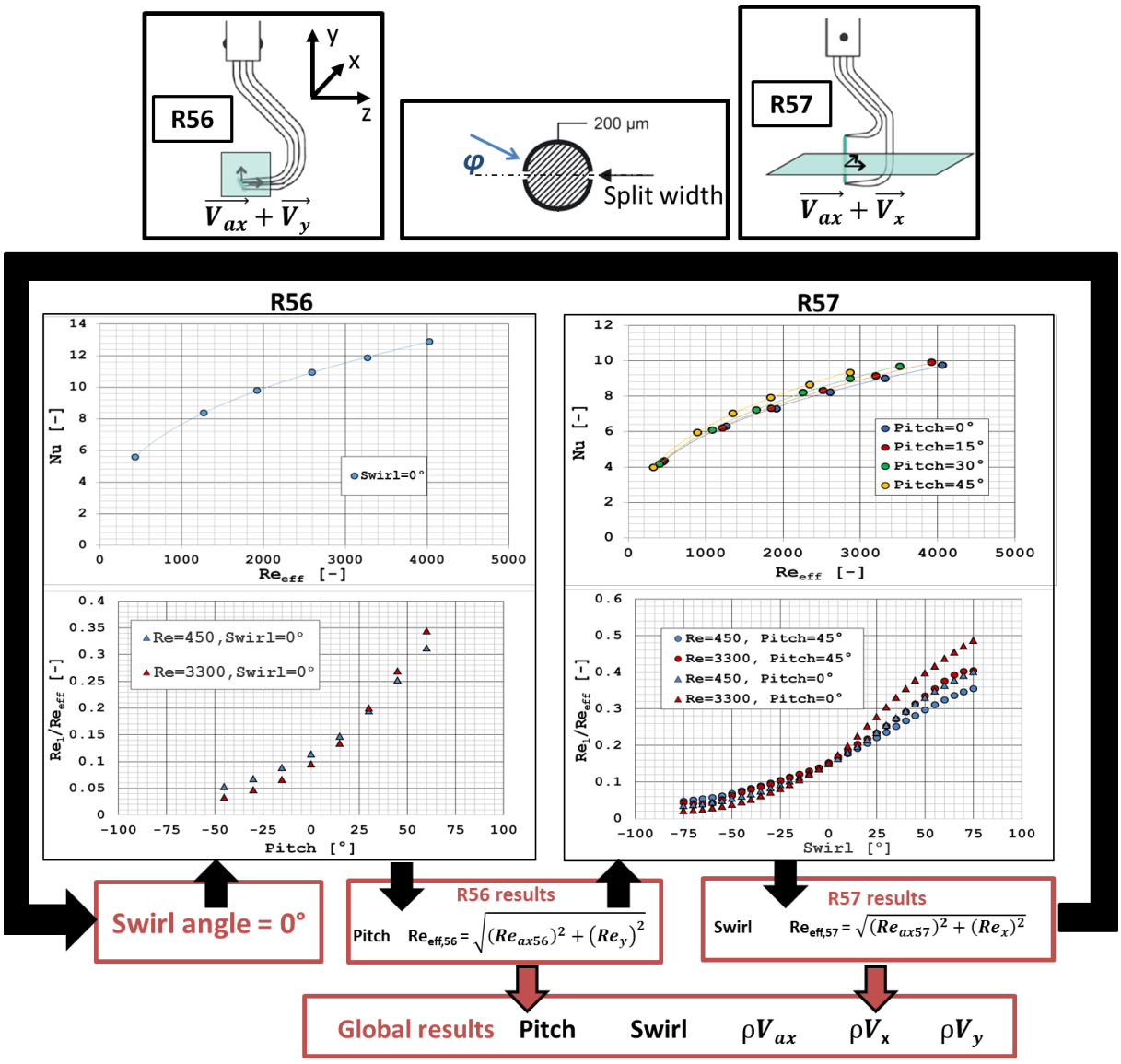

Figure 2: **HWA measurements post-process conceptual map**

post-process: the Mach number variation is very limited between the two measurement positions and its influence on the HWA results was found to be negligible at the expected Mach values. On the other hand, the HWA probe preswirl, decided on the basis of 5HP results, is only a starting point for the post-process, as sketched in Fig. 2, and possible discrepancies are corrected by the following iterations. The whole post-process can be summarized in the following steps:

- Calculation of Nu_{56} from Eq. 1 and probe 55R56 test results (i.e. output voltages). T_0 was measured using a standard thermocouple upstream of the swirlers. η_r wa evaluated through correlations (Cukurel et al. 2012), using local Mach number value from 5HP results. The mass-flux calibration for $swirl = 0°$ was used as a first step to evaluate Re_{eff} (top left plot in Fig. 2).
- Calculation of Nu_1 using Eq. 1 with E_2=0. Evaluation of pitch angle ($pitch_1$) through angular calibration curve with $swirl = 0°$ (bottom left plot in Fig. 2).
- Analogous procedures on probe 55R57 test results using the calibration curves for $pitch = pitch_1$.
- Check of evaluated time averaged swirl angle. If the swirl angle is significantly different from zero, the whole process is repeated, with the proper calibrations curves for probe 55R56 test results, until convergence is achieved.

It must be pointed out that the results are not obtained in the rig cylindrical coordinates, but in the "probe coordinates"; since the probe is moved by a cartesian traverse system and the probe coordinates depend on the imposed pre-swirl (point-by-point variable), axial, horizontal and vertical directions, so as pitch and swirl angles definition, can be different for all the points of the measurement mesh. As a result, it was not possible to obtain the time-evolution of the velocity components in the "relevant" directions. It was possible, anyway, to collect both average and statistical results and combine them, as for the turbulence intensity calculated with Eq. 2 where subscripts ax, x and y refer to probe coordinates, point by point different from each other.

$$T_u = \frac{\sqrt{\frac{1}{3}((\rho V_{ax})^2_{rms} + (\rho V_x)^2_{rms} + (\rho V_y)^2_{rms}))}}{\sqrt{((\overline{\rho V_{ax}})^2 + (\overline{\rho V_x})^2 + (\overline{\rho V_y})^2)}} \tag{2}$$

Concerning the acquisition, it was set at 10 kHz for 3 seconds after a "frequency sensitivity" evaluation procedure: different mesh points were acquired at different acquisition frequency, ranging from 2 to 50 kHz and it was found that negligible differences in the calculated Tu occurred beyond an acquisition frequency of 10 Hz.

In order to provide an evaluation of the measurements uncertainty, several points, at different velocities and flow angles, were acquired on the calibration apparatus for both the probes, and the developed post-processing procedure was applied to re-calculate the mass-flux values. Errors within 5% were found, in the flow angle range that was expected during the tests. Applying the method developed by Kline and McClintock to Eq. 2, an uncertainty up to 7% can be expected on the turbulence intensity measurements.

EXPERIMENTAL RESULTS

Mean field description

In order to allow a better interpretation of the turbulence results it is useful to discuss the overall flow field characteristics, measured by five hole probe.

Fig. 3 shows the results on Plane 40, in terms of non-dimensional height (h/H, y-axis) and non-dimensional tangential position (i.e. tangential coordinate t [°], made non-dimensional by the 9° NGV pitch p). The attention is paid to the flow angles pattern as well as to the total pressure, normalized by

the mass-averaged value on the measured domain ($P_{0,40}/P_{0,40,av}$). A sketch of swirl and pitch angles is also reported for the sake of a better understanding.

A clear clockwise rotation (looking from the combustor chamber towards the turbine) can be recognized: the highly swirling structure promoted by the swirler is, therefore, found to be conserved up to the NGV inlet position, despite its tangential momentum is progressively dissipated. Maximum swirl angles above 50° and pitch angles up to 60° are measured, as well as a low pressure area in the center of the rotating structure. A shift of the swirling structure core towards right, with respect to the rig centerline, can be also appreciated: this phenomenon was generated by the strongly converging inner line, that inhibits the rotation in the inner part of the annulus. It can be concluded that an aggressive swirl profile is achieved at combustor exit, which should translate in a representative turbulence pattern, to be characterized.

Concerning Plane 41, the attention was focused on the evaluation of total pressure losses and secondary flows, as it allows an effective understanding of the main phenomena to be achieved. For these reasons, total pressure contour plots, made non-dimensional by the mass-averaged value measured on Plane 40 ($P_{0,41}/P_{0,40,av}$), with overlapped secondary flow vector fields, are reported in Fig. 4a, for both the cases with and without film-cooling ($MFR = 0; 7.5\%$). The contour plots were rotated to bring the central airfoil wake to $t/p = 0$.

Due to the shift of the swirling core, revealed on the upstream plane, most of the structure passes through the right passage and is conserved up to the cascade exit. Important pressure losses can be found in correspondence of the airfoil wakes and due to endwall secondary losses. In particular, the biggest contribution can be identified on the suction side end of the inner endwall area of the lateral profile (NGV3), where the residual swirl directly collides with the passage vortex. A low total pressure area can be also appreciated in the right passage, in the center of the residual swirling structure, similarly to what was evidenced on Plane 40 (Fig. 3). Concerning the comparison between the two reported coolant conditions, higher profile losses can be appreciated at MFR=7.5%, as well as a lower total pressure in the right passage, presumably due to the interaction between the injected coolant and the rotating structure. To get a more in-depth analysis and a more quantitative comparison, one-dimensional profiles of the 2D vorticity on the measurement plane have been calculated at three different annulus heights and reported in Fig. 4b. Positive values of vorticity correspond to clockwise rotation, coherent with the residual swirling structure. Despite the plots of the two different coolant conditions look quite similar to each other, some differences can be appreciated. The vorticity peaks at $h/H = 50\%$ and 80% suggest

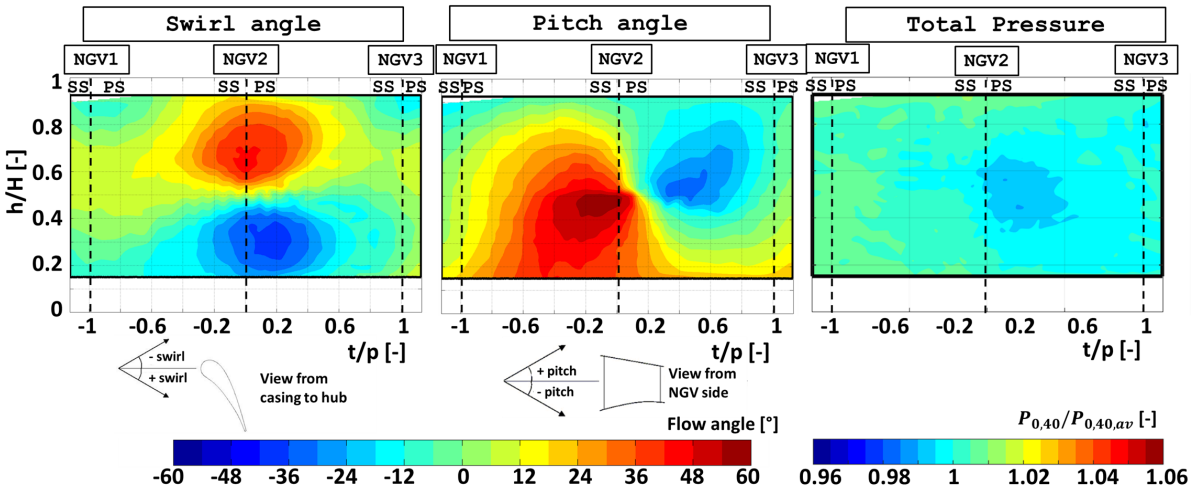

Figure 3: **Overall flow field measured by five hole probe traversing on Plane 40**

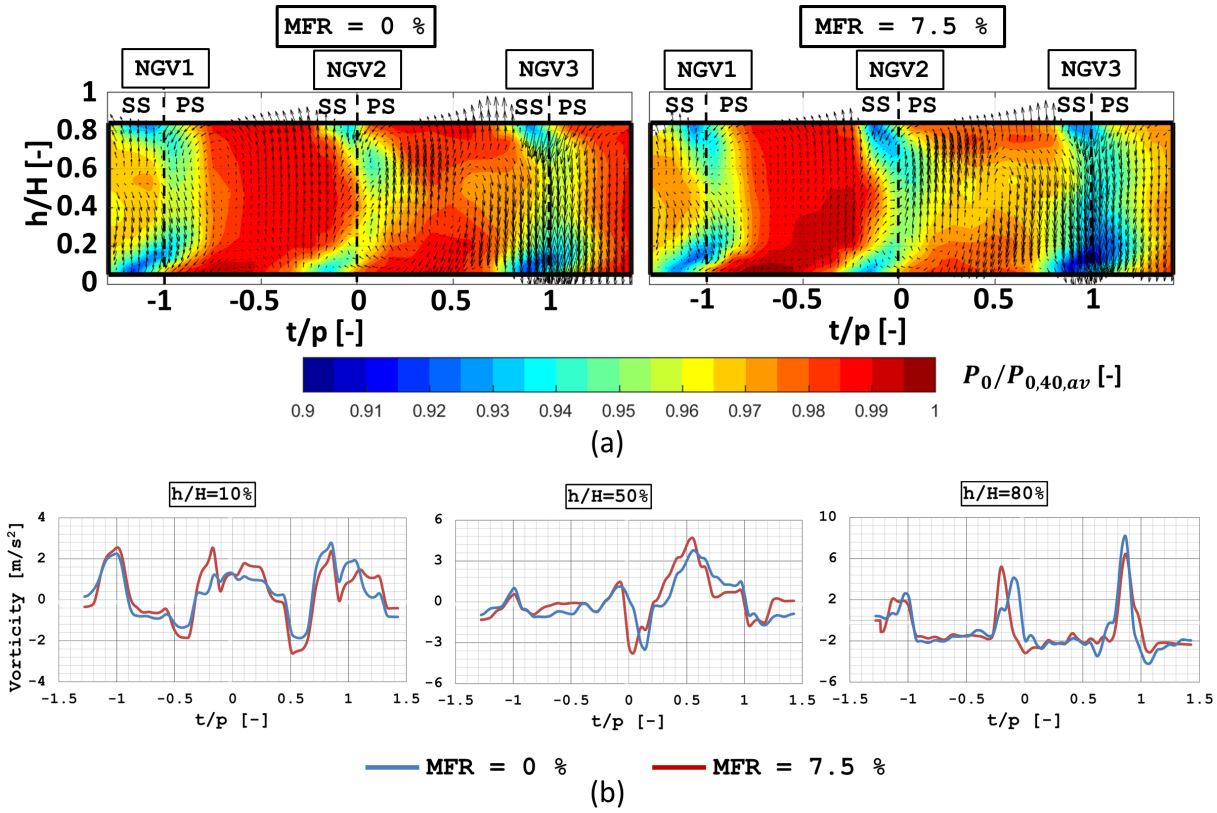

Figure 4: **Overall flow field measured by five hole probe traversing on Plane 41 (a) and vorticity 1D profiles (b)**

that the mutual interaction between coolant and mainflow alters the shape and the position of the residual rotating structure in the right passage. In particular the vorticity peaks are shifted towards the left by the presence of the cooling flow. As a result, the different position of the rotating structure has a different impact on the interaction with the typical near wall secondary flows. For instance, the cooled condition increases the negative peak of vorticity at $h/H = 10\%$, $t/p \approx 0.5$, suggesting a different interaction of the swirling structure with the inner passage vortex which seems more squeezed on the inner boundary of the investigate domain for $MFR = 0$ case. Very limited effects are recognized, on the other hand, in the left passage, less affected by the swirling flow.

Before moving to the turbulence results, since the aggressive three-dimensional flow can constitute a severe challenge to traditional hot wire measurement approaches, a validation of the reliability of the adopted technique was pursued through a comparison between mass flux measured by 5HP and HWA; the comparison is reported in Fig. 5 only for Plane 40, since it can be considered the more challenging measurement plane, due to the very high flow angles to be measured.

A reasonable agreement is achieved between the HWA and 5HP, especially for tangential and radial components. The main difference stays in the evaluation of the axial velocity at h/H=25% and 50%, where HWA returns higher mass-flux values. However, the slight different axial position of the plane of measurements can have a strong impact in comparing the axial velocity for the two measurement techniques, as the convergent liners should induce an axial acceleration to the flow. In order to verify this hypothesis, the results of a SAS simulation of the combustor simulator, whose details can be found in the work of Andreini et al. (2016), are also reported in the plots, for both measurement positions (HWA and 5HP plane). Despite some differences arise in the comparison between experimental and

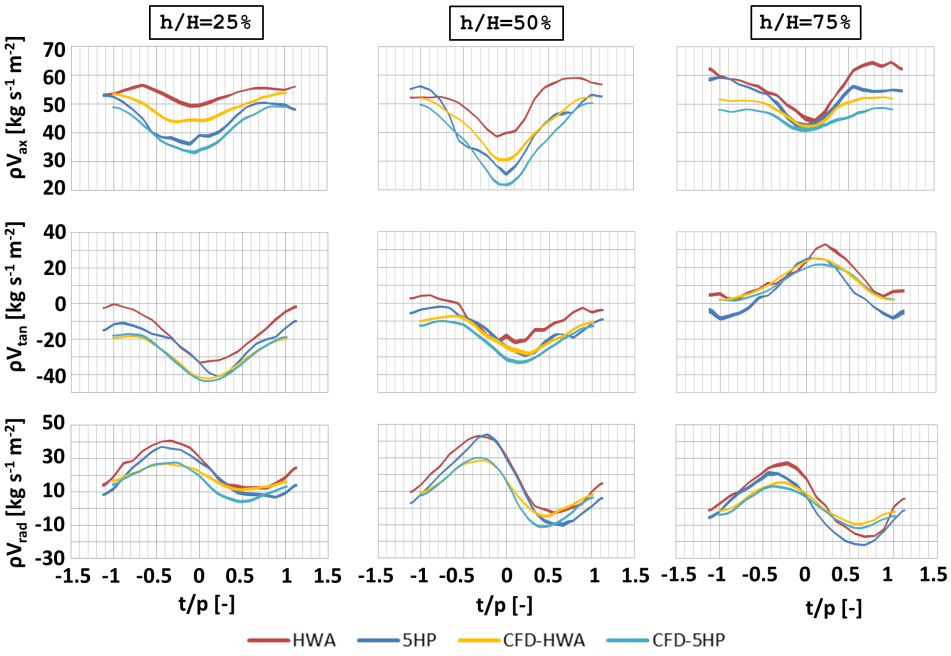

Figure 5: **Overall flow field upstream NGV: comparison between HWA, 5HP and CFD results**

numerical findings, CFD predictions return the same behaviour of the experimental results, with a strong impact of the axial plane position on ρV_{ax} component. Therefore, it seems reasonable to confirm that the highlighted discrepancies between 5HP and HWA measurements, concerning the axial mass flux, are due to the slightly different measurement plane. Since no precise quantitative conclusions can be drawn from these comparisons, Fig. 6 shows the same comparison, limited to the total mass flux values, which is the parameter actually used in Tu calculation (denominator of Eq. 2), on Plane 41, where 5HP and HWA measurements positions coincide. The results show that the differences mostly stay well within 5%, with higher values (mostly below 10%, with a local maximum of 12.5%) in correspondence of the airfoil wakes, where the five-hole probe is known to have some blockage effect, resulting in slight underestimation of the mass flux (as confirmed by a Filtered Rayleigh Scattering measurement campaign performed by Doll et al. 2018 on the same rig). The plots, therefore, confirm that the measured uncertainty correspond to what was estimated during the calibration phase and prove the validity of the HWA methodology in resolving the flow field and hence to provides a reliable estimation of the 3D

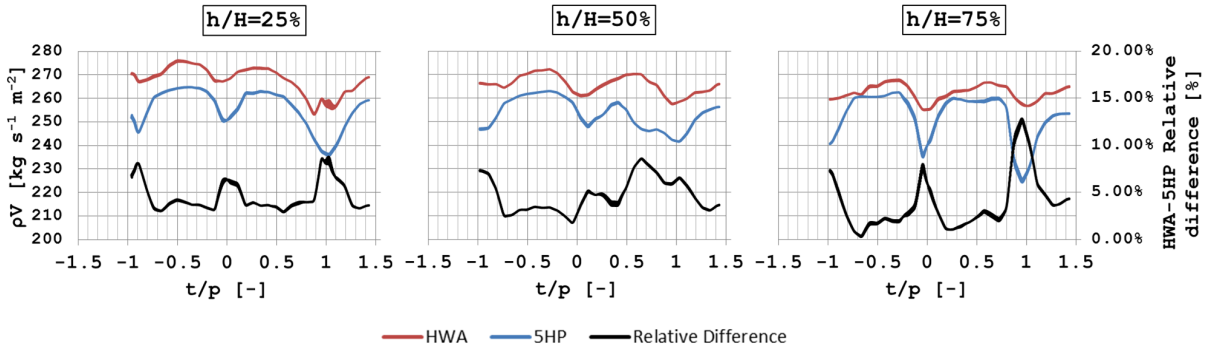

Figure 6: **Overall flow field downstream NGV: comparison between HWA and 5HP results**

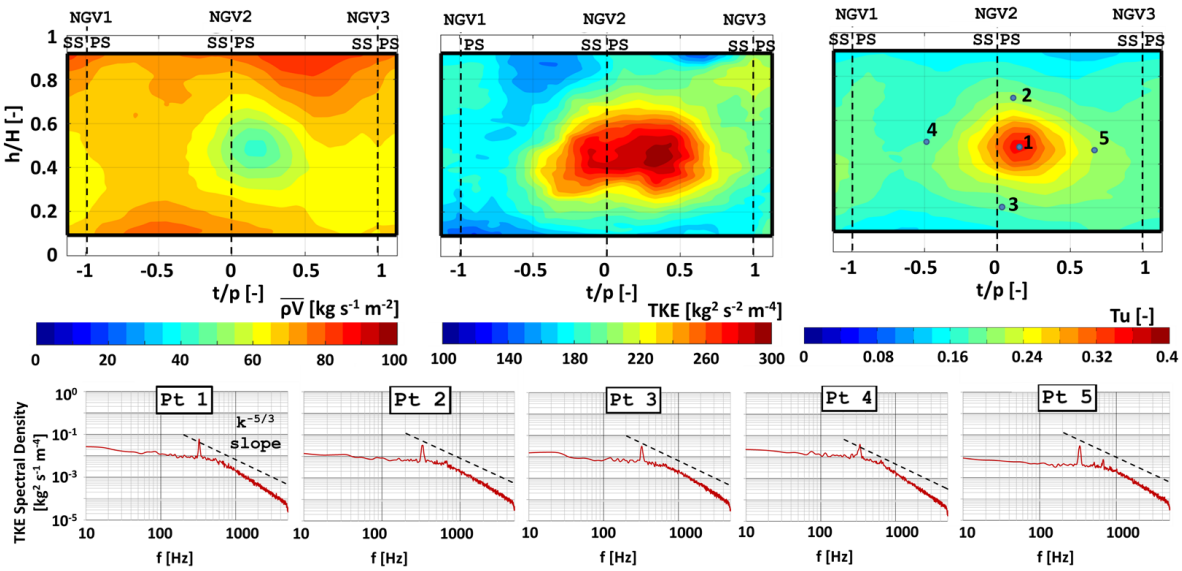

Figure 7: **Turbulence intensity and TKE spectral density on Plane 40**

kinetic energy and turbulence intensity.

Turbulence intensity

Despite the combustor simulator tested in the present work is not able to reproduce unsteady phenomena linked to reactive processes, it is known that the gross of the turbulence intensity, for lean combustor, should follow the swirl profiles (Hall et al. 2013; Lubbock and Oldfield 2017) and the aerodynamic field. For this reason the following experimental results in terms of turbulence quantities could represent valuable data to help in the NGV design in engines that adopt lean burn combustors.

Plane 40

Fig. 7 shows the turbulence intensity contour plot measured on Plane 40, as well as the average mass flux and a mass-flux TKE, that contribute to the calculation of Tu (Equation 2) in the top 2D plots:

$$TKE = \frac{1}{2}((\rho V_{ax})^2_{rms} + (\rho V_x)^2_{rms} + (\rho V_y)^2_{rms}) \tag{3}$$

The map shows a well-defined high-turbulence spot, where values reach about 35%, which perfectly corresponds to the position of the swirling core center. As it is shown by the first two contour plots, this very high value is generated both by the low local velocity and by the enhanced velocity fluctuations in the vortex core. It is pretty clear, therefore, that most of the turbulence intensity contribution, as expected, is generated by the highly swirling structure promoted by the swirler that reaches the combustor exit. Even if no significant turbulence intensity areas can be found in the top and in the bottom parts of the annulus, the investigated domain is not close enough to the walls to provide proof that no important contributions come due to the interaction between the mainflow and the liner coolant layers.

The evaluation of turbulence intensity gives an idea of the overall kinetic energy per unit mass associated with the turbulent flow eddies; beside that, it is also interesting to investigate how this energy is distributed among different scales. To do so the Fourier Transform has been applied to the three mass flux fluctuating components and the turbulent kinetic energy, for every frequency, has been calculated using the following relation:

$$TKE(f_i) = \frac{1}{2}((\rho V^{'}_{ax}(f_i))^2 + (\rho V^{'}_{x}(f_i))^2 + (\rho V^{'}_{y}(f_i))^2) \tag{4}$$

where f_i is a frequency value between 0 and 5000 Hz with a resolution of 1/3 Hz. The frequency spectra, depicted in the bottom plots of Fig. 7, have been averaged on steps of 10 Hz in order to have a clear view of their trend. The variable on the y-axis is the spectral density $E(f_i) = TKE(f_i)/df$, where df is the resolution step on the frequency axis. With such a visualization, the area under the curve between two frequencies f_1 and f_2 represents the turbulent kinetic energy associated to that frequency range. The turbulent spectral density is shown for five different points, whose position in the measurements plane is reported in the top right contour; they correspond to the points of maximum turbulence, maximum and minimum swirl and maximum and minimum pitch, moving respectively from point 1 to point 5. A lot of other locations were investigated showing very similar results. A typical trend that is commonly associated to turbulent flows can be recognized, with TKE progressively decreasing as the turbulent frequency is increased (i.e. as the lengthscale decreases). A curve with a $k = 5/3$ slope is also reported in order to compare the measured trend with the one obtained from Kolmogorov hypothesis. The matching is quite good, at $f > 500Hz$, for all the reported points. Beside the common trend, a clear peak can be observed for all points, at $f = 324 - 334Hz$, generated by swirling flow unsteady structure (PVC). The energy contribution of this phenomenon is responsible for only a reduced amount of the global TKE (ranging from 4 to 7% depending on the considered mesh point). Therefore it can be concluded that the main part of the turbulent kinetic energy measured at combustor exit is not due to a single unsteady structure, but due to the swirl-induced broadband unsteadiness of the flow field.

Plane 41

Once the turbulence intensity at the NGV inlet has been detailed, it is possible to evaluate how it is modified across the cascade and assess its values and pattern at the rotor inlet position. Fig. 8 shows the mass flux, TKE and turbulence intensity contour plots measured on Plane 41, together with the tangentially averaged ($-1 < t/p < 1$) 1D profiles, at different cooling flow conditions. First of all, the comparison clearly shows that an important reduction in the turbulence intensity occurs, as the focus moves from Plane 40 to 41. While values above 30% were measured upstream of the cascade, they do not exceed 5% downstream of it, as expected due to the severe acceleration of the flow field. Nevertheless these limited values are far to be considered negligible. Even if a very limited number of works have dealt with the quantification of Tu reduction across a cascade, the methodology developed by Steelant and Dick (1999) could be used as a reference, as also evidenced by Boyle et al. (2002). They postulated that in traditional cases with uniform turbine inflow the upstream-downstream turbulence intensity ratio varies as the velocity ratio to the three-halves power:

$$\frac{Tu_{40}}{Tu_{41}} = (\frac{V_{41}}{V_{40}})^{3/2} \tag{5}$$

In the investigated test case, this approach would predict, on Plane 41, a maximum turbulence intensity (starting from the maximum value of 35% measured on Plane 40) of 3% and an average value (starting from the average value on Plane 40 of 19%) below 2%, significantly underestimating the measured quantities.

Moreover, the analysis of the plots evidences important differences with respect to the typical conclusions drawn by experiments with uniform inlet flow field: in that cases higher turbulence intensities are recognized in the wakes of the airfoils and in correspondence of the passage vortexes, both at inner and outer endwalls, due to their mixing with the mainflow (Dossena et al. 1993; Boyle et al. 2002; Porreca et al. 2007). In the present test case, spots with relevant turbulence intensity can be actually found, in the inner part of the annulus, where the interaction between mainflow and inner passage vortex occurs. Even if they are evident for both the central and the lateral airfoils, a slightly higher turbulent intensity is measured for the right spot, in agreement with the highlighted behaviour of the residual swirl, directly colliding with the endwall flow structure. The extension of the investigated area does not allow the visualization of any presence of similar structures close to the outer endwall. Beyond the spots close

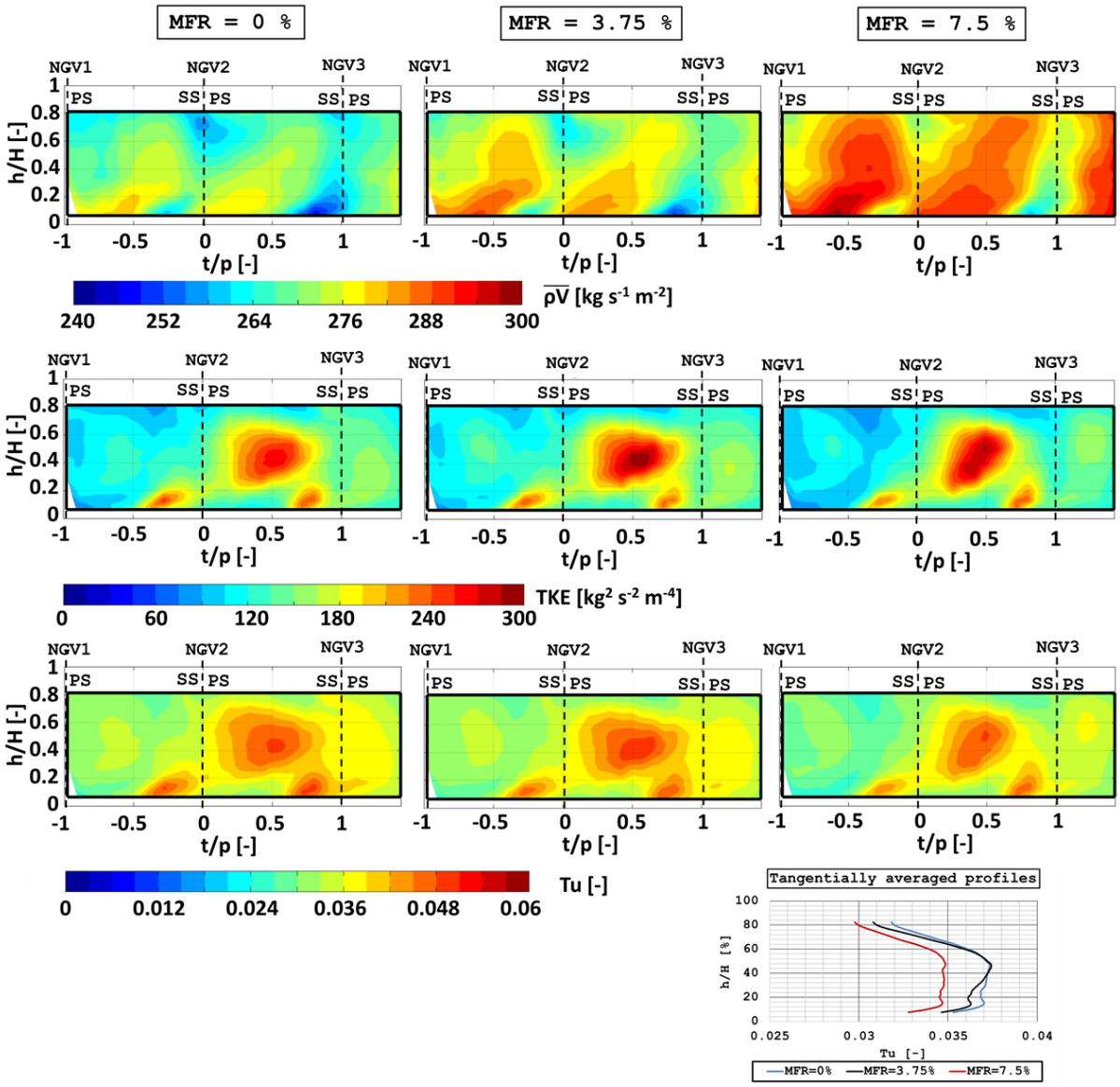

Figure 8: **Turbulence intensity on Plane 41**

to the hub, no particular evidence of high turbulence intensity in the trailing edge wakes can be found. Even if this contribution strongly depends on the distance between the trailing edge and the investigated position, it is clear that it is not the main source of turbulence at the rotor inlet plane. On the other hand, a very important contribution is provided by the high turbulence spot measured at the NGVs inlet, that is convected downstream and it is clearly visible in right passage, where, according to the mean flow field results, the residual swirling structure was detected.

Concerning the comparison between the different coolant conditions, the mass flux results allow higher velocities to be appreciated, as coolant mass flow is injected: since the same conditions are pursued on Plane 40, for all the tested cooling conditions, the addition of film cooling results in an enhanced acceleration across the cascade; despite that, the variations in the average Mach number (see Table 1) is very limited so that no significant modifications of the aerodynamic behaviour should be expected due to this aspect. The TKE plots evidence an enhancement of the velocity fluctuation moving from MFR=0%

to MFR=3.75%, especially in the swirling core, presumably due to interactions between film-cooling flows and rotating structure. At MFR=7.5% no further TKE enhancement can be found, while the shape and the position of the turbulent spot looks different as a result of the interactions between coolant and the swirling structure previously highlighted by the vorticity contour plots. The high-TKE spots close to the inner endwall, on the other hand, do not exhibit any relevant TKE enhancement, although the injection of the coolant has an impact on the interaction region between swirl and endwall secondary flow as already discussed looking to the mean flow field. All these aspects contribute to the outcomes in terms of turbulence intensity: its value is very similar between MFR=0% and 3.75%, while the effect of a significant film-cooling mass flow rate injection on the swirling flow behaviour, together with the slight flow acceleration, result in lower turbulence intensity for the case with MFR=7.5%.

Even if the differences are quite limited a clear trend of turbulence intensity reduction with increasing coolant mass flow rate can be also appreciated from the tangentially averaged profiles, with a quite flat pattern at mean radius positions.

CONCLUSIONS

The experimental analysis showed that the turbulence intensity pattern at the combustor simulator exit is mainly dominated by the effect of a swirling structure promoted by the swirler and conserved up to Plane 40. For this reason a very high turbulence intensity (up to 35%) can be detected in the very center of the swirling flow. The TKE spectral density profiles clearly show the presence of the processing vortex core, responsible for a limited contribution to the overall TKE. Downstream of the NGV cascade the residual swirling structure convected in the right passage is the main driving phenomenon affecting the turbulence profile. High turbulent intensity values were appreciated in the center of the residual swirling flow and in the locations where it interacts with secondary endwall flows, determining significantly different behaviour from what is normally expected in traditional test cases with uniform inlet flow conditions. Despite a reduction in TKE across the cascade, important values, up to about 5%, were measured on Plane 41. The measured Tu values on P41 are higher than what can be evaluated through a prediction approach developed for uniform turbine inflow. Moreover the resulting turbulence pattern present significant distortions in tangential and radial directions, pointing out to highly non-uniform local inlet conditions for the rotor cascade, both in space and time. This behaviour suggests that particular attention must be paid in rotor cascade design, accounting for the actual 2D turbulence pattern, in order to avoid dangerous underestimations of the heat transfer rates. On the other hand, the effect of film cooling injection is such that a slight reduction in TKE is achieved, as the cooling flows interact with the coherent swirling flow, affect its evolution and reduce its large scale turbulence.

ACKNOWLEDGEMENTS

The authors wish to gratefully acknowledge FACTOR (Full Aerothermal Combustor-Turbine interactiOns Research) Consortium for the kind permission of publishing the results herein. FACTOR is a Collaborative Project co-funded by the European Commission within the Seventh Framework Programme (2010-2016) under the Grant Agreement n° 265985. The authors also wish to gratefully acknowledge MIUR (Italian Office for University and Research) for partially financing the research within Research National Program PRIN 2010-11, for the project INSIDE “Aerothermal Investigation of cooled Stage turbine: Design optimization and Experimental analysis”.

REFERENCES

Ames, F. (1994), ‘Experimental study of vane heat transfer and aerodynamics at elevated levels of turbulence’, *NASA Contractor’s Report 4633* .

Ames, F. (1997), ‘The influence of large-scale high-intensity turbulence on vane heat transfer’, *ASME J. Turbomach.* **9(1)**, 23–30.

Andreini, A., Bacci, T., Insinna, M., Mazzei, L. and Salvadori, S. (2016), 'Hybrid rans-les modeling of the aerothermal field in an annular hot streak generator for the study of combustor-turbine interaction', *ASME J. Eng. Gas Turb. Power* **139**(2), 021508.

Bacci, T., Becchi, R., Picchi, A. and Facchini, B. (2018), 'Adiabatic effectiveness on high pressure turbine nozzle guide vanes under realistic swirling conditions', *ASME J. Turbomach.* **141**(1), 011009.

Bacci, T., Caciolli, G., Facchini, B., Tarchi, L., Koupper, C. and Champion, J. (2015), 'Flowfield and temperature profiles of a combustor simulator dedicated to hot streaks generation', *ASME Conference Proceedings* (GT2015-42217).

Bacci, T., Lenzi, T., Picchi, A., Mazzei, L. and Facchini, B. (2018b), 'Flow field and hot streak migration through high pressure cooled vanes with representative lean burn combustor outflow', *ASME J. Eng. Gas Turb. Power* **141**(4), 041020.

Boyle, R., Lucci, B. and Senyitko, R. (2002), 'Aerodynamic performance and turbulence measurements in a turbine vane cascade', *ASME Conference Proceedings* (GT2002-30434).

Cukurel, B., Acarer, S. and Arts, T. (2012), 'A novel perspective to high-speed cross-hot-wire calibration methodology', *Experiments in Fluids* **53**, 1073–1085.

Doll, U., Dues, M., Bacci, T., Picchi, A., Stockhausen, G. and Willert, C. (2018), 'Aero-thermal flow characterization downstream of an ngv cascade by five-hole probe and filtered rayleigh scattering measurements', *Experiments in Fluids* **59**(10), 150.

Dossena, V., Perdichizzi, A., Ubaldi, M. and Zunino, P. (1993), 'Turbulence measurements downstream of a turbine cascade at different incidence angles and pitch-chord ratios', *ASME Conference Proceedings* .

Ekkad, S. V. and Han, J. C. (2000), 'A transient liquid crystal thermography technique for gas turbine heat transfer measurements', *Measurement Science and Technology* **11**, 957–968.

Fossen, G. V. and Bunker, R. (2001), 'Augmentation of stagnation heat transfer due to turbulence from a dln can combustor', *ASME J. Turbomach.* **123**, 140–146.

Hall, B. F., Chana, K. S. and Povey, T. (2013), 'Design of a non reacting combustor simulator with swirl and temperature distortion with experimental validation', *ASME Conference Proceedings* (GT2013-95499).

Huu, E. and Beguier, C. (1995), 'Velocity measurements in 3d turbulent flows by means of a rotating x-wire probe', *Meas. Sci. Technol.* **6**, 843–850.

Jenkins, S., Varadarajan, K. and Bogard, D. G. (2004), 'The effects of high mainstream turbulence and turbine vane film cooling on the dispersion of a simulated hot streak', *ASME J. Turbomach.* **126**(1), 203–211.

Kergourlay, G., Kouidri, S., Rankin, G. and Rey, R. (2006), 'Experimental investigation of the 3d unsteady flow field downstream of axial fans', *Flow Measurement and Instrumentation* **17**, 303–314.

Koupper, C., Caciolli, G., Gicquel, L., Duchaine, F., Bonneau, G., Tarchi, L. and Facchini, B. (2014), 'Development of an engine representative combustor simulator dedicated to hot streak generation', *ASME J. Turbomach.* **136**(11), 111007–111007.

Lubbock, R. and Oldfield, M. (2017), 'Turbulent velocity and pressure fluctuations in gas turbine combustor exit flows', *Proc IMechE Part A: J Power and Energy* **0**(0), 1–13.

Nasir, S., Carullo, J. S., Ng, W.-F., Thole, K. A., Wu, H., Zhang, L. J. and Moon, H. K. (2009), 'Effects of large scale high freestream turbulence and exit reynolds number on turbine vane heat transfer in a transonic cascade', *ASME J. Turbomach.* **131**, 021021–021021.

Pena, F. and Arts, T. (1994), 'The rotating slanted hot wire anemometer in practical use', *Proceedings of the 2nd International Conference on Experimental Fluid Mechanics* .

Porreca, L., Hollenstein, M., Kalfas, A. and Abhari, R. (2007), 'Turbulence measurements and analysis in a multistage axial turbine', *AIAA Journal of Propulsion and Power* **23**(1), 227–234.

Radomsky, R. W. and Thole, K. A. (1999), 'Flowfield measurements for a highly turbulent flow in a stator vane passage', *ASME J. Turbomach.* **122**(2), 255–262.

Schmid, G., Krichbaum, A., Werschnik, H. and Schiffer, H. (2014), 'The impact of realistic inlet swirl in a 1-1/2 stage axial turbine', *ASME Conference Proceedings* (GT2014-26716).

Steelant, J. and Dick, E. (1999), 'Prediction of by-pass transition by means of a turbulence weighting factor - part i: Theory and validation', *ASME Conference Proceedings* (99-GT29).

Werschnik, H., Hilgert, J., Wilhelm, M., Bruschewski, M. and Schiffer, H. (2017), 'Influence of combustor swirl on endwall heat transfer and film cooling effectiveness at the large scale turbine rig', *ASME J. Turbomach.* **139(8)**.